Cross-comparison of global simulation models applied to Mercury's dayside magnetosphere

S. Aizawa [a,b,*], L.S. Griton [a,k], S. Fatemi [c,d], W. Exner [e,f,g], J. Deca [h,i,j], F. Pantellini [k], M. Yagi [l], D. Heyner [e], V. Génot [a], N. André [a], J. Amaya [m], G. Murakami [n], L. Beigbeder [o], M. Gangloff [a], M. Bouchemit [a], E. Budnik [p], H. Usui [q]

[a] IRAP, CNRS-CNES-UPS, Toulouse, France
[b] Graduate School of Science, Tohoku University, Sendai, Japan
[c] Swedish Institute of Space Physics, Kiruna, Sweden
[d] Department of Physics at Umeå University, Umeå, Sweden
[e] Institute for Geophysics and Extraterrestrial Physics, Technische Universität Braunschweig, Braunschweig, Germany
[f] Institute for Theoretical Physics, Technische Universität Braunschweig, Braunschweig, Germany
[g] School of Earth and Atmospheric Sciences, Georgia Institute of Technology, Atlanta, USA
[h] Laboratory for Atmospheric and Space Physics (LASP), University of Colorado Boulder, Boulder, CO, 80303, USA
[i] Institute for Modeling Plasma, Atmospheres and Cosmic Dust, NASA/SSERVI, CA, 94035, USA
[j] Laboratoire Atmosphères, Milieux, Observations Spatiales (LATMOS), Université de Versailles à Saint Quentin, 78280, Guyancourt, France
[k] LESIA, Observatoire de Paris, Université PSL, CNRS, Sorbonne Université, Université de Paris, 5 place Jules Janssen, 92195, Meudon, France
[l] RIKEN, Kobe, Japan
[m] CmPA, Mathematics Department, KU Leuven, Belgium
[n] ISAS/JAXA, Sagamihara, Japan
[o] GFI, Toulouse, France
[p] Noveltis, Toulouse, France
[q] Kobe University, Kobe, Japan

ARTICLE INFO

ABSTRACT

We present the first comparison of multiple global simulations of the solar wind interaction with Mercury's dayside magnetosphere, conducted in the framework of the international collaborative project SHOTS - Studies on Hermean magnetosphere Oriented Theories and Simulations. Two 3D magnetohydrodynamic and two 3D hybrid simulation codes are used to investigate the global response of the Hermean magnetosphere without its exosphere to a northward-oriented interplanetary magnetic field. We cross-compare the results of the four codes for a theoretical case and a MESSENGER orbit with similar upstream plasma conditions. The models agree on bow-shock and magnetopause locations at 2.1 ± 0.11 and 1.4 ± 0.1 Mercury planetary radii, respectively. The latter locations may be influenced by subtle differences in the treatment of the plasma boundary at the planetary surface. The predicted magnetosheath thickness varies less between the codes. Finally, we also sample the plasma data along virtual trajectories of BepiColombo's Magnetospheric and Planetary Orbiter. Our ability to accurately predict the structure of the Hermean magnetosphere aids the analysis of the onboard plasma measurements of past and future magnetospheric missions.

1. Introduction

Mercury is a planet of extremes that is continuously battered by a harsh and dynamic solar wind. Combined with interplanetary magnetic field (IMF) magnitudes up to 30 nT and a small Parker spiral angle, Mercury's weak internal magnetic field produces a unique

magnetosphere in the solar system (Ness et al., 1975; Whang, 1977; Korth et al., 2018; Slavin et al., 2018; Jang et al., 2020). For example, the Hermean magnetosphere is twenty times smaller in volume than Earth's magnetosphere and Mercury's volume fraction in its magnetosphere is approximately five hundred times larger than the equivalent terrestrial number (Slavin et al., 2008, 2009a, 2010). As a result, the solar wind can

---

* Corresponding author. IRAP, CNRS-CNES-UPS, Toulouse, France.
  E-mail address: sae.aizawa@irap.omp.eu (S. Aizawa).

directly interact with the surface, even outside the magnetospheric cusps (Winslow et al., 2013). In addition, the significant offset between the magnetic dipole origin and the center of the planet results in a surface magnetic field strength in the northern hemisphere that is double the nominal value estimated for the southern hemisphere (Slavin et al., 2014, 2019; Jia et al., 2019; Winslow et al., 2020). These particularities culminate in fascinating particle precipitation patterns and differential space weathering that is as variable as the upstream solar wind (Kallio et al., 2008; Raines et al., 2014; Fatemi et al., 2020). The absence of a significant ionosphere makes Mercury's conductive core an integral part of the electrodynamic current closure and complicates the evolution of the complex local plasma environment even more (Jia et al., 2015; Johnson et al., 2016).

Numerical simulations of the solar wind interaction with the Hermean magnetosphere have thus far adopted multi-fluid/magnetohydrodynamic (Jia et al., 2015; Kabin et al., 2000; Benna et al., 2010; Dong et al., 2019) and hybrid approaches (representing the ions as computational particles and the electron populations as a (massless) fluid) (Fatemi et al., 2017, 2018, 2020; Kallio and Janhunen, 2003, 2004; Trávníček et al., 2007, 2010; Wang et al., 2010; Richer et al., 2012; Herčík et al., 2013, 2016; Exner et al., 2018, 2020). These models, designed to focus on the ion kinetics, have been successful in recreating the general structure of Mercury's local plasma environment. For example, with a 3D hybrid model, Müller et al. (2012a) characterised a diamagnetic current system that originates from the proton pressure gradients at Mercury's inner magnetosphere to explain the day- and night-side diamagnetic decreases observed by MESSENGER (Anderson et al., 2011; Slavin et al., 2008). In addition, recent numerical developments have produced the first fully kinetic, global simulations of the Hermean magnetosphere (Peng et al., 2015a, 2015b; Chen et al., 2019).

Due to mission constraints such as limited field of view and energy range to observe ions, both the Mariner-10 and MESSENGER spacecraft were limited to measure the Hermean plasma environment and thus, to fully disentangle plasma processes such as finite-gyroradius effects and complex electron dynamics (Slavin et al., 2018). Complementary to the previous missions, BepiColombo's Magnetospheric (Mio) (Mukai et al., 2006)) and Planetary Orbiter (MPO) (Milillo et al., 2010)) allow for multi-spacecraft coordinated observations (Milillo et al., 2020). Their plasma instruments focus on direct measurements of the response of Mercury's magnetosphere and its near-space environment to dynamic changes in the solar wind, including plasma-wave-charged-particle resonances, kinetic-scale instabilities, particle distributions, and energy transfer via field-aligned currents and waves (Slavin et al., 2018).

In order to optimally prepare for the measurement campaign and to be able to fully interpret and analyse the data during the forthcoming Mercury flybys and during the orbital phase, or in other words, to exploit most efficiently the multi-point measurements allowed by the dual spacecraft and the synergies between the various sensors of the onboard plasma suite, sophisticated modeling tools are required. Hence, the SHOTS (Studies on Hermean magnetosphere Oriented Theories and Simulations) project has been established as an integral part of the BepiColombo Young Scientist Study Group. Its aim is to share and compare simulation results among the BepiColombo Science Working Team in order to prepare the scientific analysis of the in-situ magnetospheric observations gathered by Mio and MPO.

In this first comparative study, we identify the differences between fluid and hybrid simulation approaches to model the structure of the Hermean magnetosphere and its plasma environment. We compare the bow shock and magnetopause locations with a representative set of MESSENGER measurements and predict the plasma environment along virtual trajectories of BepiColombo's Mio and MPO spacecraft.

2. Model descriptions and methodology constraints

The four computer models used in this comparison study are briefly described here, with special emphasis on their inner boundary condi-

tions. We find that subtle differences in the treatment of the plasma boundary at the planetary surface affect the global solar wind - magnetosphere structure. Two magnetohydrodynamic (MHD) and two hybrid codes have been employed to identify the consequences of the different assumptions that are implemented in the physical model of the codes. In Table 1, we summarize the general numerical settings adopted for the four codes, such as the number of cells used, the size of the simulation domain, the spatial resolution, and the time step. The output from all models are stored and discussed using the Mercury Solar Orbital (MSO) frame. The X-axis points towards the Sun and the Y-axis is chosen opposite to the orbital motion of Mercury. The Z-axis points to the geophysical north and completes the right-handed coordinate system. The intrinsic magnetic field of the planet is set as a dipole with a 480 km offset towards the north from the planetary center (Anderson et al., 2012). The dipole moment is $200 \, \text{nT} \times R_M^3$. To avoid further numerical complexities, we do not include the tenuous Mercury's exosphere in our simulations just yet. In a recent hybrid study, Exner et al. (2020) investigated the kinetic effects of different sodium exosphere surface densities onto the Hermean magnetsphere. They found that an average sodium exosphere based on a realistic model of Gamborino et al. (2019) does not bring a significant change on the magnetic field structure inside the magnetosphere. Therefore, we do not include the tenuous sodium exosphere in this study.

2.1. MHD models

The three-dimensional MPI-AMRVAC (MPI-Adaptive Mesh Refinement Versatile Advection Code) code (hereafter AMRVAC) is the first three-dimensional MHD model we use in this study. This code integrates the MHD equations using a two-step Lax-Friedrichs-type scheme associated with a Woodward gradient limiter (Keppens et al., 2012; Xia et al., 2018). A Powell correction is also used to satisfy the $\nabla \cdot \mathbf{B} = 0$ condition at each time step (Powell et al., 1999). In order to limit magnetic diffusion, the magnetic field $\mathbf{B}$ is split into an analytically prescribed background field $\mathbf{B}_0$ and a residual field $\mathbf{B}_1$ (Griton et al., 2018). The full system of equations is solved on a spherical grid that is linearly spaced along the angular coordinates θ and φ and logarithmically spaced along the radial coordinate r. Hence, the simulation domain itself is a spherical shell. Note from Table 1 that only AMRVAC employs a spherical coordinate system. With a total number of cells of $(N_r, N_\theta, N_\varphi) = (36, 36, 72)$, covering the radial interval $r \in R_M [1, 10]$, the horizontal and vertical cell size near the surface are 213 km and 161 km, respectively. At the outer boundary, free slip conditions ($\partial/\partial r = 0$) are applied to all fields where the angle between the solar wind direction and the normal to the boundary direction is $< 80°$. Ambient (upstream) solar wind conditions are set at the remaining sides of the domain. At the inner boundary of the simulation domain, here the planetary surface, the radial velocity is set to zero. A free slip condition is applied to the tangential components of the momentum $\rho \mathbf{v}$. If the radial velocity immediately above the surface is positive (i.e. in case of outflow), the plasma number density and the total fluid pressure are set to $n = 30 \, \text{cm}^{-3}$ and $p = 0.1 \, \text{nPa}$, respectively. On the other hand, if the radial velocity immediately above the surface is negative (i.e. in case of inflow), n and p are allowed to evolve within 15–150 cm^{-3} and 0.1–1 nPa. A free slip condition is also applied to the normal component of $\mathbf{B}_1$ at the surface. The tangential components are set to zero. The results of AMRVAC are interpolated to a uniform Cartesian grid with a spatial resolution of $81.5^3 \, \text{km}^3$ for ease of comparison with the other simulation models.

Yagi's code is the second three-dimensional MHD model we use (Yagi et al., 2009, 2010). In this code, a Rational-CIP (Constrained Interpolation Profile) algorithm is implemented to solve the advection term (Yagi et al., 2010) and a fourth-order Runge-Kutta and a fourth-order central difference method are used to solve the non-advection terms needed to advance the numerical scheme in time and space. In contrast to AMRVAC, the magnetic vector potential $\mathbf{A}$ is computed instead of the

Table 1
Summary of the numerical settings. For AMRVAC the finest spatial resolution is quoted.

	Grid type	#cells	Domain size	Resolution	Time step	particles/cell
AMRVAC (Keppens et al., 2012)	Spherical	(36, 36, 72)	$r \in R_M$ [1, 10]	213×161 km	0.03 s	–
Yagi (Yagi et al., 2009)	Cartesian	(300, 300, 300)	$(-10{:}+6, \pm 5, \pm 5)\, R_M$	122 km	0.02 s	–
AIKEF (Müller et al., 2011)	Cartesian	(320, 224, 224)	$(-6{:}+8, \pm 9, \pm 9)\, R_M$	100 km	0.08 s	25
Amitis (Fatemi et al., 2017)	Cartesian	(234, 396, 396)	$(\pm 7, \pm 10, \pm 10)\, R_M$	125 km	0.001 s	16

magnetic field, ensuring $\nabla \cdot \mathbf{B} = 0$ by definition and a uniform Cartesian grid is adopted. In this study, the grid resolution is set to 122 km³. The simulation domain measures $(-10{:}+6, \pm5, \pm5)\, R_M$, with the number of cells of $(Lx, Ly, Lz) = (300, 300, 300)$. The inner boundary of the computational domain is the planetary surface. Mercury is treated as a reflective obstacle, allowing no flux to penetrate across the surface (obstacle). We also apply the free slip condition which does not allow any radial pressure and density gradient at the planetary surface. The inner boundary conditions accommodate a smooth convection of the magnetic field in the vicinity of the planet, mimicking obstacle with low conductivity.

2.2. Hybrid models

AIKEF (Adaptive Ion Kinetic Electron Fluid) is the first three-dimensional hybrid model we employ in this study. Contrary to MHD, a hybrid model treats ions kinetically while electrons are included as a massless charge-neutralizing fluid. In this study, the number of computational macro-particle per cell is set to 25 to represent their Maxwellian velocity distribution. The magnetic and electric fields are obtained by solving the Maxwell's equations, i.e., the electric field $\mathbf{E}$ is directly calculated from the electron momentum equation and Faraday's law, $\partial\mathbf{B}/\partial t = -\nabla \times \mathbf{E}$, is used to advance the magnetic field $\mathbf{B}$ in time. The fields propagate between the grid points with a Runge-Kutta-algorithm. AIKEF operates on a Cartesian grid and the mesh is capable of automatically adapting its resolution in regions where large field gradients exist (Exner et al., 2018; Müller et al., 2011). For simplicity, we do not activate this function here and use a fixed spatial resolution of 100 km³ instead, and the simulation domain is set to $(-6{:}+8, \pm9, \pm9)\, R_M$ with the number of cells of $(Lx, Ly, Lz) = (320, 224, 224)$. To include magnetic induction processes within Mercury, Mercury's core is assumed to be highly conductive so that the resistivity in the core region is in effect set to zero. The magnetic diffusion in the mantle is facilitated by applying a maximum resistivity of $1.21 \cdot 10^7\, \Omega \cdot m$ (Jia et al., 2015; Exner et al., 2018) and employing a Crank-Nicolson algorithm. The resistivity profile is smoothed at the surface and core-mantle-boundary in an identical way as in Jia et al. (2015). Mercury's surface is treated as a perfect plasma absorber, i.e., particles impacting the surface are removed. To ensure numerical stability, 0.2% of smoothing parameter is applied between the grid points (Müller et al., 2012b).

The Amitis is a GPU-based (Graphics Processing Units) three-dimensional hybrid model of plasma that currently runs only on a single CPU-GPU pair (Fatemi et al., 2017). It has been developed to reduce the computational resources that are typically needed for running global simulations and resulted in performance enhancement of 10x-100× over its CPU-based predecessor. As with AIKEF, the model kinetically tracks positively charged macro-particles, i.e., the ion population, by solving the Lorentz equation of motion while using a fluid description for massless electrons. The electric field and magnetic field are obtained by solving Maxwell's equations. The model is grid-based and uses regular-spaced, cell-center Cartesian grids to solve all the equations. We choose a spatial resolution of 125 km³ with 16 macro-particles per cell, and simulation domain is set to $(\pm7, \pm10, \pm10)\, R_M$. The model self-consistently couples the geophysical, induced electromagnetic response of the interior of a planetary body to the electromagnetic response of the incident plasma and magnetic fields by solving Maxwell's equations for the plasma and a magnetic diffusion equation $(\partial\mathbf{B}/\partial t = -\nabla$

$\times \nabla \times \mathbf{B}/\mu_0\sigma)$ for the interior of the object, where μ_0 is the permeability of free space and σ is the conductive profile for the interior of the planetary body (Fatemi et al., 2017). Amitis adopts periodic outer boundary conditions for its particles and electromagnetic fields along the axes perpendicular to the solar wind flow. Parallel to the flow the code continuously injects solar wind ions at the most upstream grid cell. The downstream boundary, identical to its implementation of the planetary surface, is a perfect plasma absorber. Unlike AIKEF, a smoothing routine is not applied in Amitis.

When plasma impacts onto the surface, a vacuum is formed in the downstream regions. In contrast to MHD codes where a minimum charge density is impose in these regions of vacuums to enable the continued calculation of the field equations, hybrid models need special handlings of the vacuum regions. AIKEF employs ghost-ions with the same charge-to-mass ratio as solar wind ions but in tenuous densities to propagate the electric and magnetic fields in the vacuum regions. This approach enables a smooth density profile at the vacuum region edges without large gradients, while also increasing the numerical resource usage due to the handling of an additional species (Trávníček et al., 2010). A different approach is used in Amitis, where, each time step, the cells within the vacuum regions obtain a flat resistivity value. This approach allows for the emergence of localized currents that propagate the electric and magnetic fields instead of ions. The vacuum state of the cells is checked every time step which does not increase numerical resources by a significant amount. However, this approach leads to unphysical resistivity gradients throughout the downstream regions that might lead to unphysical currents. Therefore, the resistivity value is capped at $10^7\, \Omega$ m to limit the resistivity gradients. As both approaches result in good agreement with spacecraft data (Fatemi et al., 2018; Exner et al., 2018), we do not investigate how these approaches relate to each other in this study.

2.3. Common visualization tools

We use netCDF as a multidimensional format with meta information for all simulations. It allows us to have a unified format for comparative visualizations, data interoperability and reusability. In the present study, we employ Paraview for 3D data visualization and analysis. In addition, we use 3Dview and AMDA (Automated Multi-Dataset Analysis), which makes use of the SPASE (Space Physics Archive Search and Extract) simulation data model (Jacquey et al., 2010; Génot et al., 2010, 2018; Roberts et al., 2018). Using SPICE kernels, 3Dview is a 3D JAVA tool that provides visualizations of the positions and attitudes of planetary missions and bodies in combination with observational data, simulations, and analytical models. AMDA is an online database and analysis tool in which in-situ observations, ground based observations, and models can be browsed, manipulated and downloaded (a workspace is available for each user). AMDA and 3Dview are developed by the CDPP (Center de Données de la Physique des Plasmas) and available to contributing developers under a GPLv3 licence.

3. Science cases

In this work we discuss two cases: (*a*) a classical textbook case under purely northward IMF conditions to obtain the characteristics of each code, and (*b*) a direct comparison with a pre-selected MESSENGER orbit.

3.1. Case a: northward IMF

Northward IMF conditions are chosen to anticipate a stable dayside magnetosphere structure. Typically, a southward IMF gives rise to more unstable magnetosphere conditions as continuous dayside magnetic reconnection in combination with a relatively short Dungey cycle does not allow the system to relax (Slavin et al., 2019). In the case of a northward IMF, the reconnection sites move to high latitudes near the magnetospheric cusps.

We set the typical solar wind condition around 0.3 AU, e.g., IMF magnitude to 20 nT and adopt a solar wind proton density of 30 cm^{-3}, an Alfvén Mach number of 5 and a total plasma beta (β) of 1.3. The solar wind speed measures 400 km s^{-1} (Sarantos et al., 2001; Winslow et al., 2013). The MHD models assume a total density equal to the proton density, whereas the plasma temperature (43 eV) is set to the sum of the electron (21.5 eV) and proton (21.5 eV) temperatures (Table 2) (Marsch et al., 1982; Sarantos and Slavin, 2009).

3.2. Case b: MESSENGER comparison

We select a MESSENGER orbit that allows a simulation setup as close as possible to our theoretical northward IMF case. Due to its mid-day to midnight orientation (X-Z plane), orbit 1415 (November 8, 2012) provides a close comparison. The orbit has a Disturbance Index of less than 25 (Anderson et al., 2013), the lowest magnetic activity quartile, the Z-components of the IMF at the inbound an outbound bow shock crossings are positive and within 2 nT of each other, and the IMF variability along the entire orbit is less than 10 nT. Combining these parameter values indicate stable solar wind conditions.

We use the inbound part of the orbit to compute the average IMF vector to be inserted in our models. Further, the Alfvén Mach number is set to 5, the solar wind speed equals 459 km s^{-1} and the proton and electron temperature measure 12 eV, and 18 eV, respectively (Marsch et al., 1982; WilsonLynn et al., 2018).

4. Results

4.1. Case a: northward IMF

A purely northward IMF configuration provides a stable magnetosphere configuration. We let each model run for 5 min, that is, 5 Dungey cycles, to reach their respective quasi-stationary states. Fig. 1 shows the solar wind proton density maps in the $X - Z$ (top) and $X - Y$ (bottom) plane on a logarithmic scale, including also velocity lines. The two left panels are the results from the MHD codes while the two right panels present the results from the hybrid codes. All models have converged to a very similar global structure for the Hermean magnetosphere and the

characteristic features are present: the shape of bowshock, the higher density magnetosheath, and the magnetospheric cusps. However, the models do not agree on the proton density near the planet and inside the nightside magnetosphere. We also observe different locations of the magnetopause structure.

The $X - Z$ cut of AMRVAC (Fig. 1, upper left-most panel) shows a less sharp shock structure at the bow shock, a low density dayside magnetosphere, patches of higher density close to the surface in the cusp (which is defined by the magnetic field topology) and tail regions, and an asymmetric structure for the nightside magnetosphere. The latter is uniquely present in AMRVAC. The model also has the largest magnetopause flaring angle among the four models. The $X - Y$ cut of AMRVAC (bottom left-most panel) shows a symmetric density structure in the dawn-dusk plane. Yagi's MHD code in the $X - Z$ plane (upper middle-left panel) presents a sharper bow shock as compared to AMRVAC, most likely due to the model's less diffusive scheme. In addition, the dayside magnetosphere is not dilute and houses a similar density as the magnetosheath. The nightside structure is more symmetric and slightly tilted northward. The density concentration we find near the tail region in the AMRVAC model is not present here. The $X - Y$ cut of Yagi's model (bottom middle-left panel) also shows symmetric structure. Compared to AMRVAC, AMRVAC shows more detailed structure than that of Yagi's. Finally, only Yagi's model results show a north-south symmetric cusp region. The $X - Z$ cut of AIKEF (upper middle-right panel), similar to Yagi and Amitis, produces a sharp bowshock and a more dilute dayside magnetosphere region. Both hybrid codes concur on narrower cusps as compared to the MHD models which visually identified. The structure in the nightside is tilted slightly northward, similar to Yagi's model. AIKEF in the $X - Y$ plane (bottom middle-right panel) shows small asymmetric structure in the density, e.g., higher density inside the magnetosphere in the dawnside while lower density appears in the duskside.

Amitis does not employ any smoothing routines. Operating with a lower number of particles per cell as compared to AIKEF, the density maps in the $X - Z$ plane (upper right-most panel) therefore seem to contain more numerical noise. However, the bowshock and magnetopause are clearly captured and the solar wind plasma is denied from penetrating through the dayside magnetosphere as in the other simulations. The narrow cusp structure is similar to the results from AIKEF. The density configuration at the nightside of the planet seems to tend to northward. Contrary to AIKEF, the $X - Y$ cut (bottom right-most panel) shows the opposite trend, e.g., the dayside magnetosphere seems to tend dawnward while in the nightside there is denser plasma close to the surface.

In order to quantify the differences between the four models, Fig. 2 presents the pressure profile along the subsolar line (X-axis). The dynamic and magnetic pressure are extracted and the locations of the bowshock and magnetopause have been identified. The four panels correspond to the four simulations. The solid lines show the dynamic (ram) pressure, $\varrho\mathbf{v}^2$ where ϱ and $\mathbf{v}$ indicate the plasma density and the bulk velocity of the upstream solar wind, while the dashed lines represent the magnetic pressure, $B^2/2\mu_0$ where B and μ_0 denote the magnetic field magnitude and the vacuum permeability, respectively. The gray dash-dotted line is the magnetic pressure produced by an uncompressed dipole magnetic field with the same dipole moment as the models, providing information on how much the planetary magnetic field is compressed by the solar wind in each simulation run. The gray vertical line at $x = 1.12\,R_M$ indicates the point where the dynamic pressure equals the uncompressed magnetic pressure and serves as a reference for the magnetopause location. For each model, the position of the bow shock (BS) has been identified as the maximum current density (red vertical solid line). The location of the magnetopause (MP; red vertical dashed line) has been identified in three different ways: (1) using the position of the most distant closed planetary field line that crosses the X-axis, (2) using the position where the gas and magnetic pressure are equal, and (3) using the position where the current density has its maximum. All three methods were in excellent agreement for all four models (Table 3).

Table 2
Summary of the common input physical and plasma parameters. *SW* denote the solar wind.

|	Case (a) Northward IMF	Case (b) MESSENGER
Planetary radius R_M [km]	2440	
Planetary dipole moment [nT $\times$ R_M^3]	200	
Northward dipole offset [km]	480	
SW proton density [cm^{-3}]	30	40
SW proton + electron temperature [eV]	21.5 + 21.5	12 + 18
SW total plasma β	1.3	0.69
SW Alfvén Mach number	5	5
SW plasma velocity [km s^{-1}]	400	459
SW Magnetosonic Mach number	3.5	8.5
IMF (X,Y,Z) components [nT]	(0, 0, + 20)	(25, −6, 4.9)
IMF magnitude [nT]	20	26.6
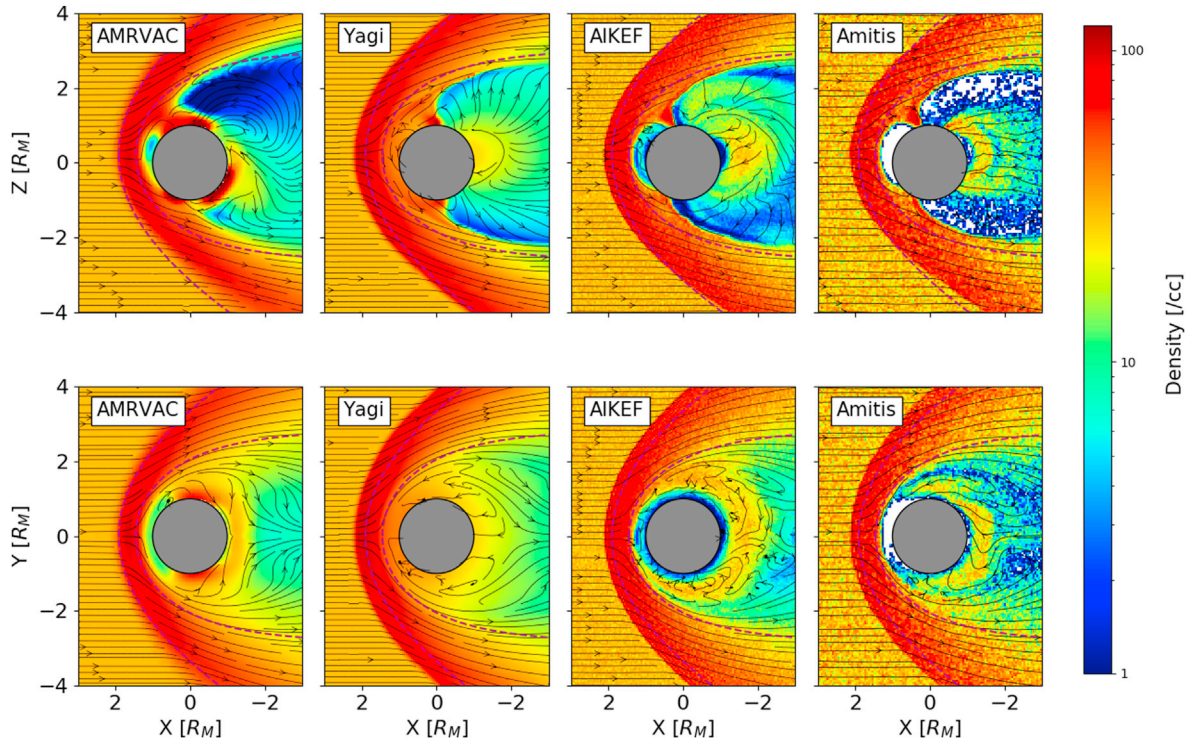
Fig. 1. Maps of the solar wind proton density in the X-Z (top) and X–Y (bottom) plane at steady-state for the four simulation models under the northward IMF (Case *a*). The two panels on the left (right) are the results from the MHD (hybrid) codes. Length scales are normalized to the Mercury radius. Black arrows show the bulk velocity stream line and dashed two curves represent the averaged location of bowshock and magnetopause obtained by MESSENGER (Winslow et al., 2013).
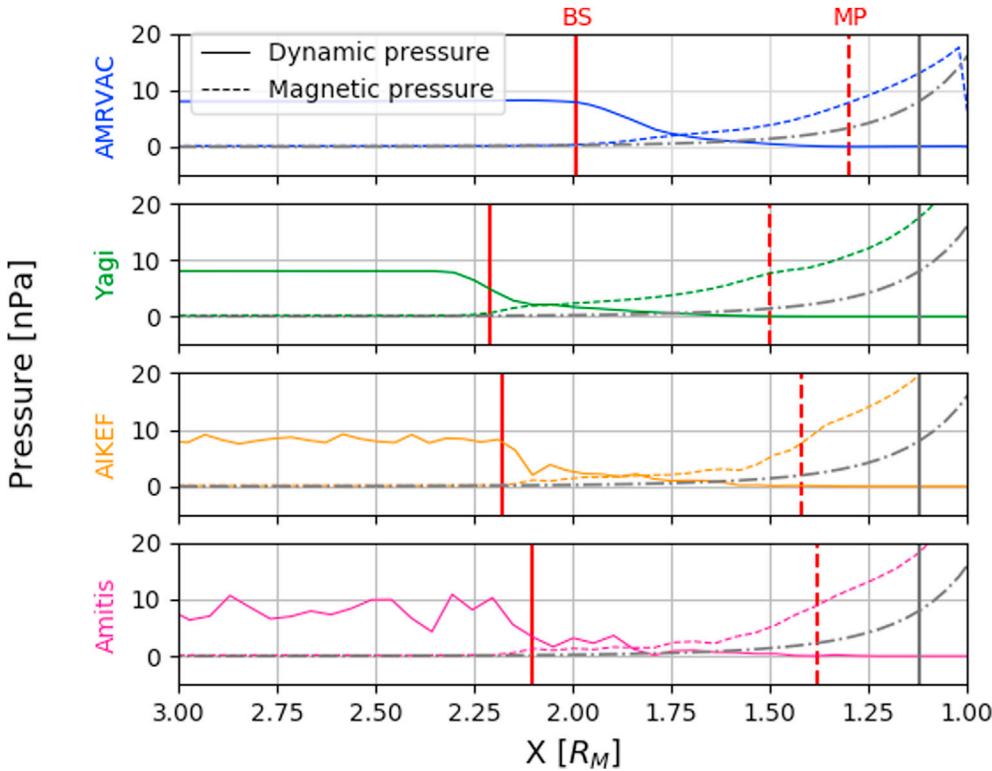

Fig. 2. Dynamic (ram) and magnetic pressure profiles along the X-axis (Sun-Mercury direction) from 3 R_M upstream to the planet surface on the dayside for the four simulation codes. The results from the two MHD codes are shown on the top two panels and the hybrid model results on the two bottom panels. The gray dash-dotted line is the magnetic pressure produced by an uncompressed dipole magnetic field with the same dipole moment as the models. The positions of the bow shock (BS) and magnetopause (MP) are shown with red vertical solid and dashed lines. The gray vertical line gives the theoretical expected position of the magnetopause in the case of a radially diminishing magnetic field.

The locations of both the bow shock and magnetopause vary among the models with a range of 0.22 R_M and 0.2 R_M, respectively (Fig. 2 and Table 3). The mean position of the bow shock and magnetopause is found at 2.12 R_M, and 1.40 R_M, with a standard deviation of $\sigma = 0.085$ and $\sigma =$ 0.072. The variation of the magnetopause location is greater than that of the bow shock as the former is more sensitive to the boundary condition applied at the surface and inside the planet. In an effort to eliminate the effects of the numerical implementation for comparison purposes, we

Table 3

Bow shock and magnetopause locations at the subsolar point, and the thickness of the magnetosheath for the four simulation models.

		BS [R_M]	MP [R_M]	Sheath thickness [R_M]	Grid size in X [R_M]
MHD	AMRVAC	1.99	1.30	0.69	0.06
	Yagi	2.21	1.50	0.71	0.05
Hybrid	AIKEF	2.18	1.42	0.76	0.04
	Amitis	2.10	1.38	0.72	0.05
Mean value		2.12	1.40	0.72	
Standard Deviation		0.085	0.072	0.026	

compute the average thickness of the magnetosheath and find 0.72 R_M with a standard deviation of 0.026. Thus, differences among models are small and within the uncertainty defined by the grid resolution. Note that the mean BS and MP locations simulated here with a purely northward IMF are within the ranges measured by MESSENGER (Winslow et al., 2013).

In addition to the bow shock and magnetopause locations along the subsolar line, we further characterize the Hermean magnetosphere by means of the reconnection sites. Fig. 3 shows a map in the $X - Z$ plane with its origin at the center of the planet. For reference, the two gray
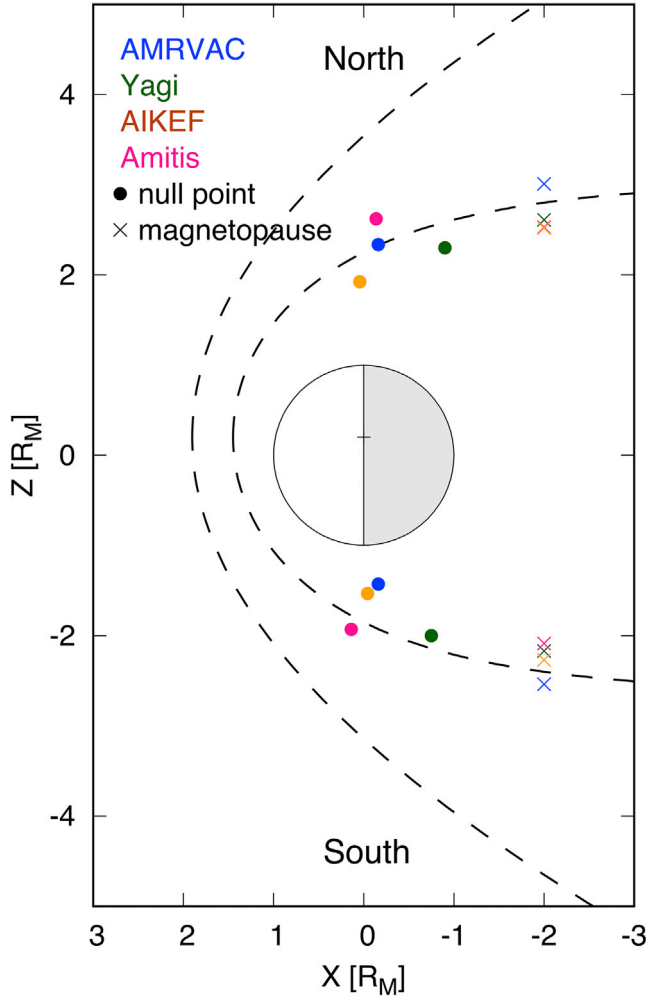
Fig. 3. The locations of null points (colored circles) and magnetopause (colored crosses) in the X-Z plane. The dashed lines show the bow shock and magnetopause models defined by Slavin et al. (Slavin et al., 2009b) and Shue et al. (Shue et al., 1997), respectively. The magnetopause paraboloid has parameters $R_{ss} = 1.45$ R_M and $\alpha = 0.5$. The bow shock model parameters are $p = 2.75$ R_M, $\varepsilon = 1.04$, and $X_0 = 0.5$ R_M.

dashed lines represent the bow shock and magnetopause locations as predicted by the models of Slavin et al. (2009b), Shue et al. (1997), Winslow et al. (2013). The positions of the reconnection sites, i.e. the null points, identified from the simulated magnetic field structure by our four models are indicated with full colored circles. The locations of the magnetopause at $X = -2$ R_M are represented with colored crosses. On average, the null points near the northern cusp are located more towards the nightside, whereas the null point near the southern cusp are clustered more towards the terminator plane (with exception of Yagi's model). Due to the dipole offset towards the north, the southern null points are closest to the planet. Note that apart from the chosen plasma field conditions also various code-specific parameters, such as numerical resistivity, may play a role in where the reconnection sites develop. AMRVAC shows the largest north-south asymmetry on the location of null points, which is consistent with the tilted magnetic structure seen in Fig. 1. The locations of the magnetopause on the nightside of the planet are obtained from the gradients of the density and the current density. With the exception of AMRVAC, these are located within the reference magnetopause model ($R_{ss} = 1.45$ R_M and $\alpha = 0.5$ where R_{ss} is the magnetopause distance at the subsolar point and α is the flaring parameter (Shue et al., 1997; Winslow et al., 2013)). Given the purely northward IMF, all four simulations can be considered in good agreement with the reference models.

Lastly in this section, the y-component of the current density in $X - Z$ plane is presented in Fig. 4. Since the IMF is purely northward, we have highlighted only the y-component of the current density. Overall, the four models display a similar appearance, i.e., the current enhancement at the bowshock, positive current at the dayside magnetopause while negative current generated along the magnetopause in other region. AMRVAC shows the thicker layer at the bowshock and magnetopause, which is likely due to the lower grid resolution and Yagi's less diffusive numerical scheme, however, on the other hand, shock locations in dayside are in good agreement with the empirical models. Yagi's code shows sharper structure in the current than that of AMRVAC and since the magnetic field structure is more symmetric in the nightside, the current structure also shows more symmetric feature. Although both two hybrid codes show more busy figure because they treat ions as the particles, it is difficult to see the peak at the dayside magnetopause. Compared to Fig. 1, since the density inside the dayside magnetosphere in AIKEF is exist but still low, those ions do not affect to the current system.

4.2. Case b: MESSENGER comparison

Fig. 5 presents overview of the plasma density, the bulk velocity, and the magnetic field in $X - Z$ plane with the MESSENGER trajectory. All model results indicate similar features and magnitudes especially in the dayside magnetosphere. Interestingly, the two hybrid models show the perturbed northern magnetopause. Fig. 6 presents the magnetic field, density and plasma velocity profile along MESSENGER orbit 1415, on the 8th of November 2012, from 4:30 UT to 10:00 UT (see also section 3.2). The spacecraft entered the magnetosphere at the nightside along a south-to north-trajectory, roughly in the meridian plane with its closest approach near the magnetic north of Mercury, thus crossing the bow shock and magnetopause twice. Four vertical black lines indicate the bow shock and magnetopause locations for both the inbound and outbound crossings observed by MESSENGER. Superimposed on their respective panels are the simulated profiles from Case *a* along the same trajectory. The red vertical lines are the averaged simulated shock crossings from the four models. Overall, our models are in close agreement with the MESSENGER data for the inbound part of the orbit. With time differences of up to 12 min, equal to ~0.28 R_M along the spacecraft trajectory for the inbound orbit, and 17 min (~1.1 R_M) for the outbound orbit, the locations of the BS and MP agree less well for the outbound section of the MESSENGER orbit. The BS locations match better for the inbound part of the orbit.

The variations of the magnetic field along the trajectory seem to be in good agreement among the codes and with MESSENGER data. On the
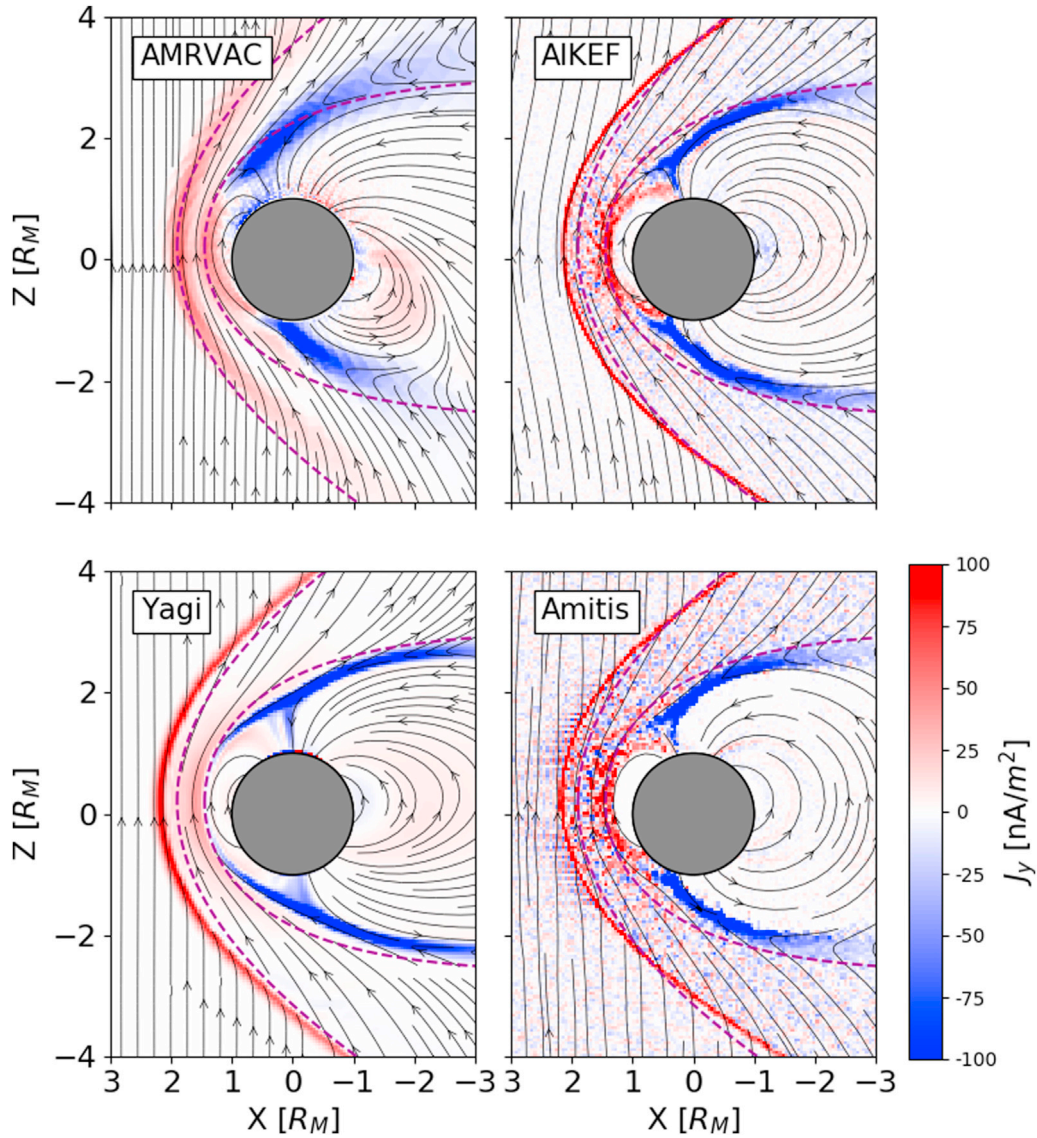
Fig. 4. The y component of the current density in $X - Z$ plane. Black lines with arrow represent the magnetic field line and dashed purple lines are the empirical models of bowshock and magnetopause.

other hand, the variations of density and bulk velocity are more diversed. The small fluctuations in two hybrid are results of particle noises.

Since we used the inbound part of the orbit to constrain the upstream plasma parameters to initialize the simulations, it is possible that variations in the solar wind dynamic pressure during the orbit may be responsible for the larger discrepancy in the outbound part of the orbit. Interestingly, there are distinct differences between the MHD and the hybrid codes (panel 4 of Fig. 6). Around 7:50 UT, when the spacecraft is inside the dayside magnetosheath, the results from the two hybrid simulations are in agreement with the observations, while both MHD models predict a lower magnetic field intensity. The spacecraft passes through the northern cusp and then moves towards the dayside region. At 8:10 UT, near the peak density, we find the compressed magnetosheath plasma. As expected, also the density and velocity profiles predicted by the hybrid codes show steeper profiles at the shock crossing compared to the MHD models.

5. Discussion

5.1. Case b: MESSENGER comparison

Due to the limited particle instrumentation on board the single-spacecraft MESSENGER mission, it is not possible to constrain the exact solar wind plasma parameters to set up a comparison simulation. More precisely, because the particle instrument onboard MESSENGER was protected by the sun shield and thus it had a limited field of view, this condition prevented the instrument from observing the majority of solar wind. Therefore, density and velocity, temperature of solar wind cannot be derived and those parameters must be assumed when input parameters were considered (Andrews et al., 2007) In addition, the solar wind varies in time and may even be changing significantly while MESSENGER crosses the magnetosphere. This may be the reason for some of the discrepancies between simulated and measured profiles. In Fig. 7 we compute the difference between the observed and modeled magnetic fields along our chosen MESSENGER orbit. We exclude the time frame between the two MP crossings (from 6:15 UT to 7:45 UT) while MESSENGER passed the nightside region of the magnetosphere (indicated by a gray background), to focus on the cusp and boundary layer locations.

Just before 5:00 UT, MESSENGER crosses the BS for the first time, about 3 min before the predicted averaged time stamp from our models. Continuing along the trajectory, both the modeled X- and Z-component agree well with MESSENGER, whereas the models underestimate the magnetic field contribution by roughly 15 nT along the Y direction. Our models agree on the inbound MP crossing time at 6:15 UT within a 5 min
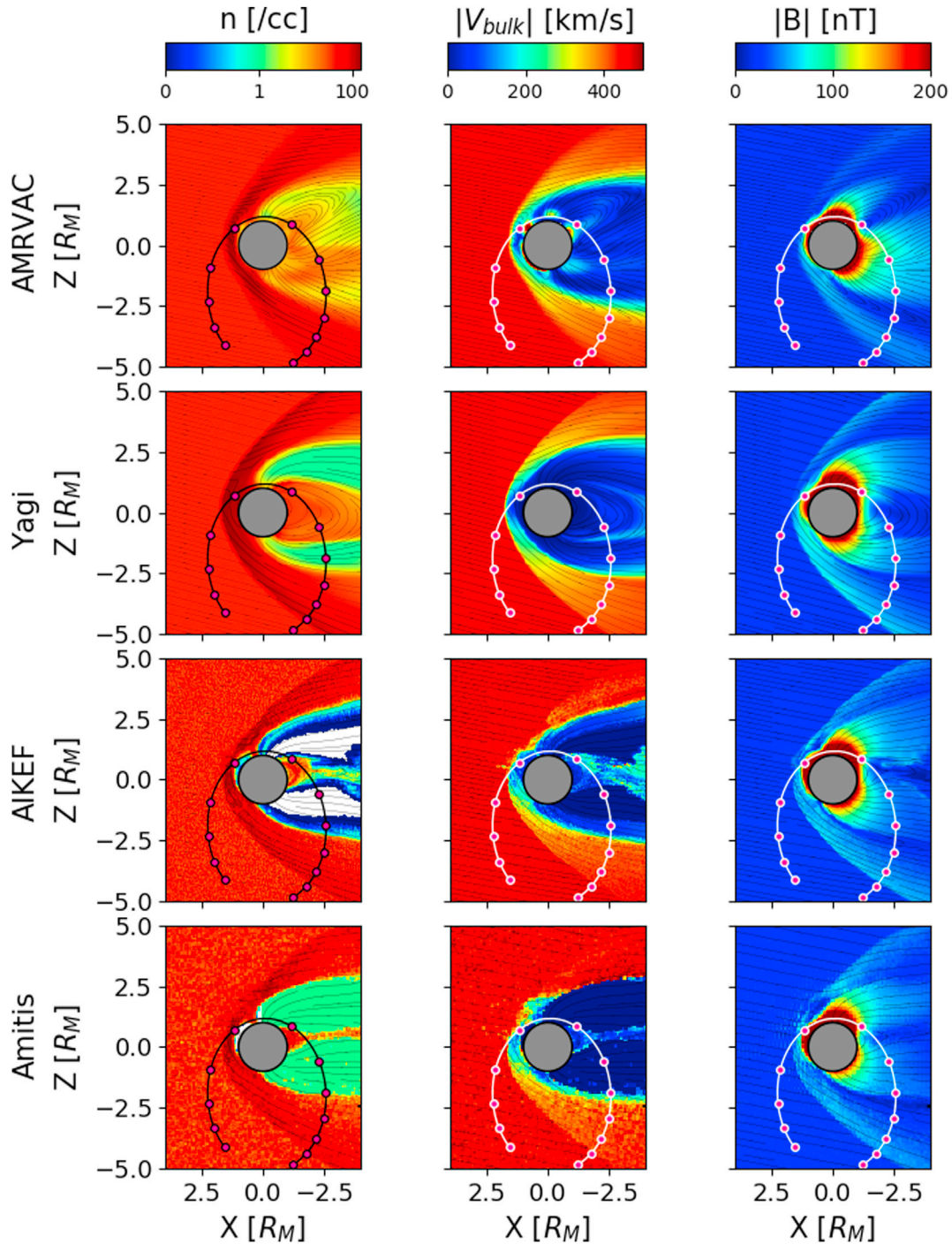
Fig. 5. The overview of Case *b*, from left to right, the panel shows the plasma density, bulk velocity, and magnitude of the magnetic field in $X - Z$ plane with magnetic field lines. MESSENGER trajectory is marked every 30 min. In this orbit, MESSENGER was first crossing the boundaries in the southern hemisphere, moving into the nightside magnetosphere.

time range. At 7:50 UT, when MESSENGER moves from the nightside to the dayside in the northern hemisphere, all four models predict a magnetic pile-up, although none of the models fully reproduces the fine-scale structure. Immediately following the pile-up, the models underestimate the magnetic field strength by roughly 100 nT. Note that the different profiles in Fig. 6 show no real 'winner' among the four simulation models as all codes show different small-scale discrepancies with the MESSENGER measurements at the boundaries between the distinct plasma regions of Mercury's magnetosphere. It shows the need for a multi-spacecraft mission, such as BepiColombo, to simultaneously

measure the local Hermean and upstream plasma environment in order to fine-tune the inputs to numerical models and in turn characterize Mercury's global plasma environment.

5.2. Virtual sampling along Mio/MPO orbits

One of the major goals of the SHOTS project, next to comparing different simulation approaches with available MESSENGER measurements, is to help prepare the community for the forthcoming BepiColombo mission by making available a catalog of simulation that
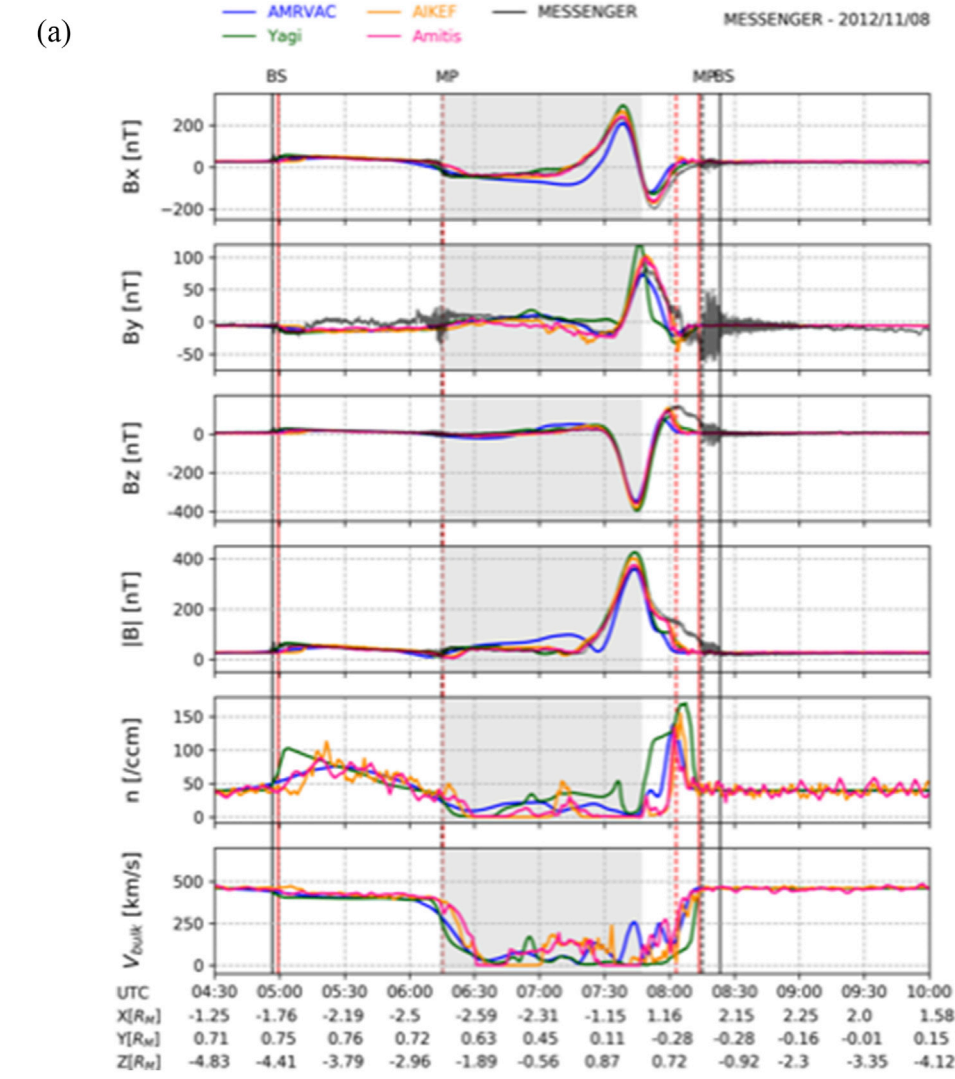
Fig. 6. (a) Modeled and observed magnetic field and modeled particle data along orbit 1415 of MESSENGER. Blue, green, orange, and red lines shows the results from AMRVAC, Yagi, AIKEF and Amitis, respectively. The black lines shows the magnetometer data measured by MESSENGER. The bow shock (BS) and magnetopause (MP) crossings identified from the observations are indicated using a vertical solid and dashed black line. The averaged simulated shock and magnetopause crossings are shown by red solid and dashed lines, respectively. The nightside magnetosphere is indicated by a gray background. (b) and (c): the trajectory of MESSENGER spacecraft in $X - Y$ and $X - Z$ plane, respectively and the dots indicate 30 min intervals of the MESSENGER trajectory.
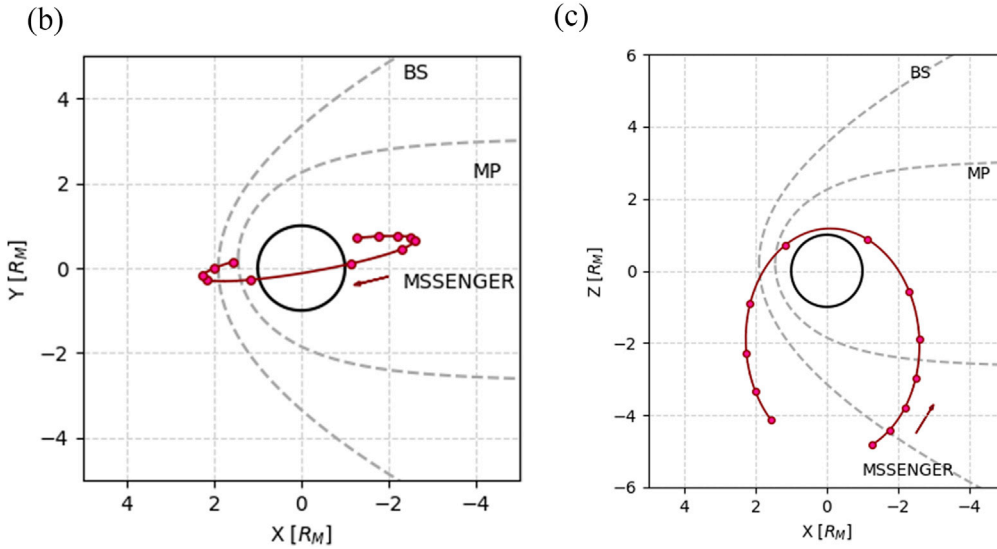
MESSENGER - 2012/11/08
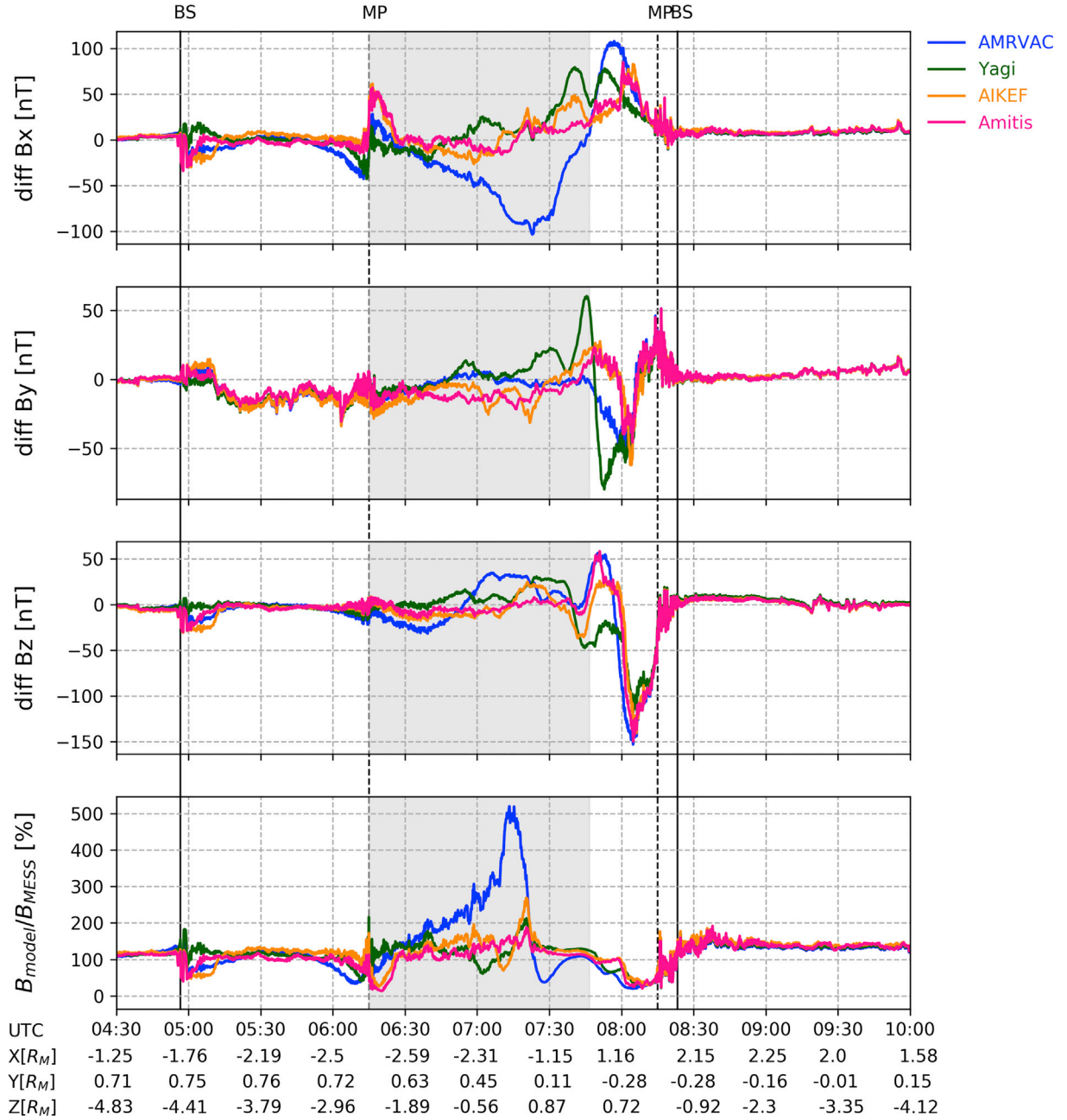
Fig. 7. Difference between the simulation results and the MESSENGER magnetic field measurements (B_{model} - B_{MESS}). The bow shock (BS) and magnetopause (MP) crossings identified by the observations are indicated by the vertical solid and dashed lines, respectively. The region MESSENGER passing through the nightside magnetosphere is indicated by a gray background.

showcases the plasma structure and dynamics of Mercury's magnetosphere under different solar wind conditions. In the first step of this project, we chose four different (MHD and hybrid) simulation models. Figs. 8 and 9 show the plasma characteristics expected along a typical Mio and MPO orbit, respectively, during the planned nominal orbital phase of BepiColombo. We chose the upstream solar wind conditions identical to the MESSENGER case studied above (Case *b* in Table 2). For ease of comparison, the orbital plane is set perpendicular to the X direction, corresponding to BepiColombo's operations planned for April 4, 2026. During this period, both Mio and MPO remain inside the magnetosphere and the plasma environment will be fully observed by the magnetometers on board Mio and MPO (Baumjohann et al., 2010; Glassmeier et al., 2010), the Mercury Plasma Particle Experiment (MPPE)

(Saito et al., 2010) and the Plasma Wave Investigation (PWI) (Kasaba et al., 2010) onboard Mio, and the Search for Exospheric Refilling and Emitted Natural Abundances (SERENA) on board MPO (Orsini et al., 2010).

In both Figs. 8 and 9 the solid vertical lines indicate the southern (T_S) and northern (T_N) terminator crossing and the dashed vertical line is the time when the spacecraft crosses the subsolar point (SSP). During this period, Mio will be moving along the frontside magnetopause (from 15:15 UT to 15:35 UT) where our models predict an enhancement of the magnetic field intensity and plasma velocity. Note that the predicted profiles closest to the planet are not in agreement, possibly due to the numerical treatment of the planetary boundary condition (see also Fig. 1). Next, Mio will move across the cusp region and re-enter the
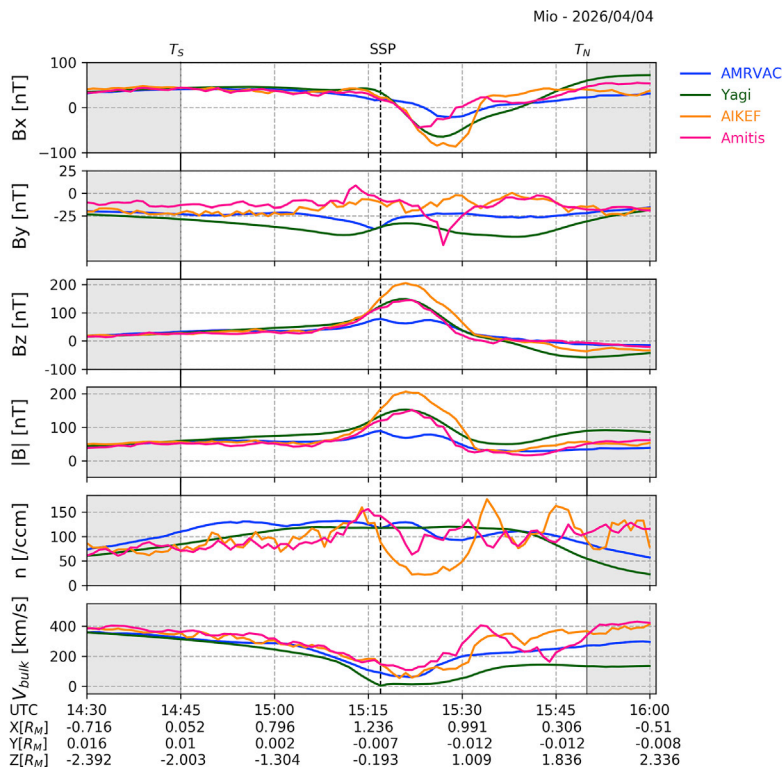
Fig. 8. Magnetic field and particle data along a representative Mio orbit. The red dots along the trajectory in the inset panel show the position of the spacecraft along 15 min intervals. The solid vertical lines indicate the crossing of the southern (T_S) and northern (T_N) terminator, the dashed vertical line is the time when the spacecraft crosses the subsolar point (SSP). The nightside region (X < 0) is indicated by a gray background.
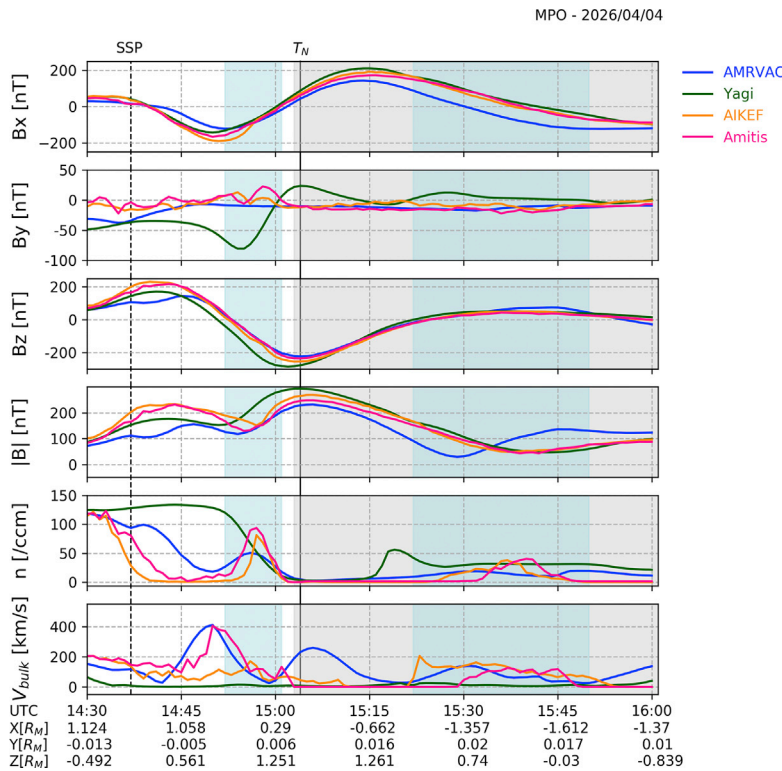

Fig. 9. Magnetic field and particle data along a representative MPO orbit. The red dots along the trajectory in the inset panel show the position of the spacecraft along 15 min intervals. The solid vertical lines indicate northern (T_N) terminator and the dashed vertical line is the time when the spacecraft crosses the subsolar point (SSP). The nightside region (X < 0) is indicated by a gray background.

nightside magnetosphere from the north. Large discrepancies among the models from around the subsolar point to the northern terminator can be explained by the orbit of the Mio spacecraft. Since Mio is moving along the magnetopause, different locations of the magnetopause in each model are critical when we extract the data along the trajectory. Mio is clearly inside the magnetopause in AIKEF and Amitis around the subsolar point but probably not in Yagi and AMRVAC. After crossing subsolar point around 15:17 UT, the density and velocity profiles diverge. A similar trend is not visible in the magnetic field predictions. This may be the region where the ion dynamics has the largest impact, i.e., the finite Larmor radius effect of particle must be taken into account in the magnetosheath, hence producing the largest differences between the hybrid and MHD models.

MPO will orbit significantly closer to the planet. The spacecraft will leave the southern magnetosphere via the nightside, then crosses the terminator and enters the dayside magnetosphere. Just before 15:00 UT and around 15:35 UT, the two hybrid models and AMRVAC predict a significant density enhancement, indicating the presence of trapped particles while Yagi shows significantly different appearance. In Yagi's model, the dayside magnetosphere is not clearly seen (see Fig. 5), and thus, the spacecraft seems to observe rather the magnetosheath component than the component inside the magnetopause at the time between 14:30 UT to 14:50 UT. The spacecraft passes through the cusp region (light blue areas in Fig. 9). MPO's trajectory will be most useful to better understand the structure and dynamics of the magnetosphere closest to the planet and in particular near the southern hemisphere. This region has been explored less due to MESSENGER's highly inclined and eccentric orbit.

Sampling the virtual orbits of Mio and MPO for a variety of solar wind parameters and/or models, we will be able to predict when the spacecraft most likely cross the cusp, the plasma sheet and the shocked regions within certain margins. These margins depend on the characteristics of the simulation and the physical processes included in the model. The combined measurements from the two spacecraft will provide a wealth of information on the Hermean plasma environment, however, to reproduce adequately the environment in 3D, numerical 3D models are essential. Thus, making predictive simulations with the information by combined spacecraft measurements is necessity to maximize the scientific return of the mission. To this effect, the simulation domain needs to be extended farther downstream of the planet to capture better the magnetotail region. Also temporal information needs to be included. In this study, our hybrid models have not implemented its exosphere based on the previous works (Kallio and Janhunen, 2004; Exner et al., 2020)that show Mercury's exosphere is too tenuous to significantly affect Mercury's magnetospheric system. Our first goal was to purely compare between MHD and hybrid simulations so that we see the ion kinetics on Mercury's magnetosphere. However, there is no doubt that revealing the role of the exosphere is also one of the key questions of Mercury's science. It will be investigated further in near future. Finally, it is stressed that Particle-In-Cell and Vlasov simulations that include the electron dynamics are needed.

6. Conclusions

We have compared the results of four different (MHD and hybrid) global simulation models with the same input parameters to simulate the solar wind interaction with Mercury's dayside magnetosphere. Because the effect of the existence of its tenuous exosphere is small to affect the structure of Mercury's magnetosphere, the exosphere has not been implemented in our models. All our models produced a similar global structure in the dayside consistent with empirical (analytical) fits for the locations of the bow shock and the magnetopause. In contrast to the dayside magnetosphere, although it is out of our scope, the magnetic field configuration in the nightside magnetosphere differs among the models, and the plasma distribution and bulk velocity close to the surface are also different. Generally speaking, MHD and hybrid models produce similar large-scale structures and commensurate plasma boundary

locations, thus, the differences between the predictions of the simulations seem to be caused numerically, i.e., the planetary boundary conditions, different size of the grid, numerical scheme, rather than the self-consistent ion kinetics included in the models.

We cross-compared our results with a theoretical northward IMF scenario (Case a) and MESSENGER orbit 1415 (Case b), indicated to have stable solar wind conditions with a northward IMF similar to the theoretical case. In Case a, the standard deviations for the predicted mean locations of the bow shock, magnetopause and the thickness of magnetosheath are small. For Case b, during the inbound part of the orbit, time differences for the bow shock and the magnetopause crossings are found up to 12 min, corresponding to a distance along the orbit of 0.28 R_M. For the outbound section of the orbit, the maximum time difference increased to 17 min, equivalent to 1.1 R_M.

One of the major goals of SHOTS is to prepare a catalog of simulations that can predict the plasma environment in- and outside the Hermean magnetosphere under different solar wind conditions, in this way contributing to maximizing the scientific return of the forthcoming BepiColombo observations. Here, for the first time, we have extracted the data from our models along representative Mio and MPO orbits. A long-lasting project-based and community-wide effort will be important both for the forthcoming BepiColombo's Mercury flybys and during its nominal orbital phase.

Author statement

Sae AIZAWA: Conceptualization, Visualization, writing-original draft preparation, writing – review & editing.

Lea S. Griton : Conceptualization, Methodology, validation, writing-original draft preparation, writing – review & editing.

S. Fatemi: Conceptualization, Methodology, validation, writing-original draft preparation, writing – review & editing.

W. Exner : Conceptualization, Methodology, validation, writing-original draft preparation, writing – review & editing.

J. Deca : writing-original draft preparation, writing – review & editing.

F. Pantellini : Methodology, validation, writing-original draft preparation, writing – review & editing.

M. Yagi: Methodology, writing-original draft preparation, writing – review & editing.

D. Heyner: Supervision, Methodology, writing – review & editing.

V. Génot: writing – review & editing, Methodology.

N. André: writing – review & editing, funding acquisition.

J. Amaya : writing-original draft preparation.

G. Murakami : Supervision.

H. Usui: Supervision.

L. Beigbeder, M. Gangloff, M. Bouchemit, E. Budnik : Technical support on Methodology.

Declaration of competing interest

The authors declare that they have no known competing financial interests or personal relationships that could have appeared to influence the work reported in this paper.

All data necessary to validate the findings presented in this manuscript can be found at https://github.com/jandeca/Aizawa_etal _PSS_2020 (DOI: 10.1016/j.pss.2021.105176) in accordance with the Findability Accessibility, Interoperability, and Reuse (FAIR) principles. The magnetometer data from the MESSENGER observations are available in the Planetary Data System (https://pds-ppi.igpp.ucla.edu).

References

Anderson, B.J., Slavin, J.A., Korth, H., Boardsen, S.A., Zurbuchen, T.H., Raines, J.M., Gloeckler, G., McNutt, R.L., Solomon, S.C., 2011. The dayside magnetospheric boundary layer at Mercury. Planet. Space Sci. 59, 2037–2050. https://doi.org/10.1016/j.pss.2011.01.010.

Anderson, B.J., Johnson, C.L., Korth, H., Winslow, R.M., Borovsky, J.E., Purucker, M.E., Slavin, J.a., Solomon, S.C., Zuber, M.T., McNutt, R.L., 2012. Low-degree structure in Mercury's planetary magnetic field. J. Geophys. Res. E: Planets 117, 1–17. https://doi.org/10.1029/2012JE004159.

Anderson, B.J., Johnson, C.L., Korth, H., 2013. A magnetic disturbance index for Mercury's magnetic field derived from MESSENGER Magnetometer data. G-cubed 14, 3875–3886. https://doi.org/10.1002/ggge.20242.

Andrews, G.B., Zurbuchen, T.H., Mauk, B.H., Malcom, H., Fisk, L.A., Gloeckler, G., Ho, G.C., Kelley, J.S., Koehn, P.L., Lefevere, T.W., Livi, S.S., Lundgren, R.A., Raines, J.M., 2007. The energetic particle and plasma spectrometer instrument on the MESSENGER spacecraft. Space Sci. Rev. 131, 523–556. https://doi.org/10.1007/s11214-007-9272-5.

Baumjohann, W., Matsuoka, A., Magnes, W., Glassmeier, K.-H., Nakamura, R., Biernat, H., Delva, M., Schwingenschuh, K., Zhang, T., Auster, H.-U., Fornacon, K.-H., Richter, I., Balogh, A., Cargill, P., Carr, C., Dougherty, M., Horbury, T.S., Lucek, E.A., Tohyama, F., Takahashi, T., Tanaka, M., Nagai, T., Tsunakawa, H., Matsushima, M., Kawano, H., Yoshikawa, A., Shibuya, H., Nakagawa, T., Hoshino, M., Tanaka, Y., Kataoka, R., Anderson, B.J., Russell, C.T., Motschmann, U., Shinohara, M., 2010. Magnetic field investigation of Mercury's magnetosphere and the inner heliosphere by MMO/MGF. Planet. Space Sci. 58, 279–286. https://doi.org/10.1016/j.pss.2008.05.019.

Benna, M., Anderson, B.J., Baker, D.N., Boardsen, S.A., Gloeckler, G., Gold, R.E., Ho, G.C., Killen, R.M., Korth, H., Krimigis, S.M., Purucker, M.E., McNutt, R.L., Raines, J.M., McClintock, W.E., Sarantos, M., Slavin, J.A., Solomon, S.C., Zurbuchen, T.H., 2010. Modeling of the magnetosphere of Mercury at the time of the first MESSENGER flyby. Icarus 209, 3–10. https://doi.org/10.1016/j.icarus.2009.11.036.

Chen, Y., Toth, G., Jia, X., Slavin, J., Sun, W., Markidis, S., Gombosi, T., Raines, J., 2019. Studying dawn-dusk asymmetries of Mercury's magnetotail using mhd-epic simulations. J. Geophys. Res.: Space Phys. submitted for publication.

Dong, C., Wang, L., Hakim, A., Bhattacharjee, A., Slavin, J.A., DiBraccio, G.A., Germaschewski, K., 2019. Global ten-moment multifluid simulations of the solar wind interaction with mercury: from the planetary conducting core to the dynamic magnetosphere. Geophys. Res. Lett. 46, 11,584–11,596. https://doi.org/10.1029/2019GL083180 arXiv:1904.02695.

Exner, W., Heyner, D., Liuzzo, L., Motschmann, U., Shiota, D., Kusano, K., Shibayama, T., 2018. Coronal mass ejection hits Mercury: A.I.K.E.F. hybrid-code results compared to messenger data. Planet. Space Sci. 153, 89–99.

Exner, W., Simon, S., Heyner, D., Motschmann, U., 2020. Influence of mercury's exosphere on the structure of the magnetosphere. J. Geophys. Res. (Space Phys.) 125, e27691. https://doi.org/10.1029/2019JA027691.

Fatemi, S., Poppe, A.R., Delory, G.T., Farrell, W.M., 2017. Amitis: a 3D GPU-based hybrid-PIC model for space and plasma physics. J. Phys. Conf. 837, 012017.

Fatemi, S., Poirier, N., Holmström, M., Lindkvist, J., Wieser, M., Barabash, S., 2018. A modelling approach to infer the solar wind dynamic pressure from magnetic field observations inside Mercury's magnetosphere. Astron. Astrophys. 614, A132. https://doi.org/10.1051/0004-6361/201832764.

Fatemi, S., Poppe, A.R., Barabash, S., 2020. Hybrid simulations of solar wind proton precipitation to the surface of Mercury. J. Geophys. Res.: Space Phys. 125, e2019JA027706 https://doi.org/10.1029/2019JA027706.

Génot, V., Jacquey, C., Bouchemit, M., Gangloff, M., Fedorov, A., Lavraud, B., André, N., Broussillou, L., Harvey, C., Pallier, E., Penou, E., Budnik, E., Hitier, R., Cecconi, B.,

Dériot, F., Heulet, D., Pinçon, J.L., 2010. Space weather applications with CDPP/ AMDA. Adv. Space Res. 45, 1145–1155. https://doi.org/10.1016/j.asr.2009.11.010.

Gamborino, Diana, et al., 2019. Mercury's subsolar sodium exosphere: an ab initio calculation to interpret MASCS/UVVS observations from MESSENGER. Ann. Geophys. 37, 455–470. https://doi.org/10.5194/angeo-37-455-2019.

Génot, V., Beigbeder, L., Popescu, D., Dufourg, N., Gangloff, M., Bouchemit, M., Caussarieu, S., Toniutti, J.P., Durand, J., Modolo, R., André, N., Cecconi, B., Jacquey, C., Pitout, F., Rouillard, A., Pinto, R., Erard, S., Jourdane, N., Leclercq, L., Hess, S., Khodachenko, M., Al-Ubaidi, T., Scherf, M., Budnik, E., 2018. Science data visualization in planetary and heliospheric contexts with 3DView. Planet. Space Sci. 150, 111–130. https://doi.org/10.1016/j.pss.2017.07.007.

Glassmeier, K.H., Auster, H.U., Heyner, D., Okrafka, K., Carr, C., Berghofer, G., Anderson, B.J., Balogh, A., Baumjohann, W., Cargill, P., Christensen, U., Delva, M., Dougherty, M., Fornaçon, K.H., Horbury, T.S., Lucek, E.A., Magnes, W., Mandea, M., Matsuoka, A., Matsushima, M., Motschmann, U., Nakamura, R., Narita, Y., O'Brien, H., Richter, I., Schwingenschuh, K., Shibuya, H., Slavin, J.A., Sotin, C., Stoll, B., Tsunakawa, H., Vennerstrom, S., Vogt, J., Zhang, T., 2010. The fluxgate magnetometer of the BepiColombo mercury planetary orbiter. Planet. Space Sci. 58, 287–299. https://doi.org/10.1016/j.pss.2008.06.018.

Griton, L., Pantellini, F., Meliani, Z., 2018. Three-dimensional magnetohydrodynamic simulations of the solar wind interaction with a hyperfast-rotating uranus. J. Geophys. Res.: Space Phys. 123, 5394–5406. https://doi.org/10.1029/2018JA025331.

Herčík, D., Trávníček, P.M., Johnson, J.R., Kim, E.-H., Hellinger, P., 2013. Mirror mode structures in the asymmetric hermean magnetosheath: hybrid simulations. J. Geophys. Res.: Space Phys. 118, 405–417. https://doi.org/10.1029/2012JA018083.

Herčík, D., Trávníček, P.M., Štverák, Š., Hellinger, P., 2016. Properties of hermean plasma belt: numerical simulations and comparison with messenger data. J. Geophys. Res.: Space Phys. 121, 413–431. https://doi.org/10.1002/2015JA021938. URL: https://agupubs.onlinelibrary.wiley.com/doi/abs/10.1002/2015JA021938.

Jacquey, C., Génot, V., Budnik, E., Hitier, R., Bouchemit, M., Gangloff, M., Fedorov, A., Cecconi, B., André, N., Lavraud, B., Harvey, C., Dériot, F., Heulet, D., Pallier, E., Penou, E., Pinçon, J.L., 2010. AMDA, automated multi-dataset analysis: a web-based service provided by the CDPP. Astrophys. Space Sci. Proc. 11, 239–247. https://doi.org/10.1007/978-90-481-3499-1_16.

Jang, E., Zhao, J.T., Yue, C., Zong, Q.G., Liu, Y., Liu, Z.Y., 2020. Energetic ion dynamics near the cusp region of mercury. Astrophys. J. 892, 10. https://doi.org/10.3847/1538-4357/ab74d1.

Jia, X., Slavin, J.A., Gombosi, T.I., Daldorff, L.K.S., Toth, G., van der Holst, B., 2015. Global mhd simulations of Mercury's magnetosphere with coupled planetary interior: induction effect of the planetary conducting core on the global interaction. J. Geophys. Res.: Space Phys. 120, 4763–4775. https://doi.org/10.1002/2015JA021143.

Jia, X., Slavin, J.A., Poh, G., DiBraccio, G.A., Toth, G., Chen, Y., Raines, J.M., Gombosi, T.I., 2019. Messenger observations and global simulations of highly compressed magnetosphere events at Mercury. J. Geophys. Res.: Space Phys. 124, 229–247. https://doi.org/10.1029/2018JA026166. URL: https://agupubs.onlinelibrary.wiley.com/doi/abs/10.1029/2018JA026166.

Johnson, C.L., Philpott, L.C., Anderson, B.J., Korth, H., Hauck, S.A., Heyner, D., Phillips, R.J., Winslow, R.M., Solomon, S.C., 2016. MESSENGER observations of induced magnetic fields in Mercury's core. Geophys. Res. Lett. 43, 2436–2444. https://doi.org/10.1002/2015GL067370.

Kabin, K., Gombosi, T., DeZeeuw, D., Powell, K., 2000. Interaction of Mercury with the solar wind. Icarus 143, 397–406. https://doi.org/10.1006/icar.1999.6252.

Kallio, E., Janhunen, P., 2003. Modelling the solar wind interaction with Mercury by a quasi-neutral hybrid model. Ann. Geophys. 21, 2133–2145. https://doi.org/10.5194/angeo-21-2133-2003.

Kallio, E., Janhunen, P., 2004. The response of the hermean magnetosphere to the interplanetary magnetic field. Adv. Space Res. 33, 2176–2181. https://doi.org/10.1016/S0273-1177(03)00447-2. URL: http://www.sciencedirect.com/science/article/pii/S0273117703004472 (mercury, Mars and Saturn).

Kallio, E., Wurz, P., Killen, R., McKenna-Lawlor, S., Milillo, A., Mura, A., Massetti, S., Orsini, S., Lammer, H., Janhunen, P., 2008. On the impact of multiply charged heavy solar wind ions on the surface of Mercury, the Moon and Ceres. Planet. Space Sci. 56, 1506–1516. https://doi.org/10.1016/j.pss.2008.07.018.

Kasaba, Y., Bougeret, J.-L., Blomberg, L., Kojima, H., Yagitani, S., Moncuquet, M., Trotignon, J.-G., Chanteur, G., Kumamoto, A., Kasahara, Y., Lichtenberger, J., Omura, Y., Ishisaka, K., Matsumoto, H., 2010. The plasma wave investigation (pwi) onboard the bepicolombo/mmo: first measurement of electric fields, electromagnetic waves, and radio waves around Mercury. Planet. Space Sci. 58, 238–278. https://doi.org/10.1016/j.pss.2008. 07.017 (comprehensive Science Investigations of Mercury: The scientific goals of the joint ESA/JAXA mission BepiColombo).

Keppens, R., Meliani, Z., van Marle, A.J., Delmont, P., Vlasis, A., van der Holst, B., 2012. Parallel, grid-adaptive approaches for relativistic hydro and magnetohydrodynamics. J. Comput. Phys. 231, 718–744. https://doi.org/10.1016/j.jcp.2011.01.020.

Korth, H., Anderson, B.J., Johnson, C.L., Slavin, J.A., Raines, J.M., Zurbuchen, T.H., 2018. Structure and configuration of Mercury's magnetosphere. In: Solomon, S.C., Nittler, L.R., Anderson, B.J. (Eds.), Mercury: the View after MESSENGER. Cambridge University Press, pp. 430–460.

Marsch, E., Schwenn, R., Rosenbauer, H., Muehlhaeuser, K.H., Pilipp, W., Neubauer, F.M., 1982. Solar wind protons: three-dimensional velocity distributions and derived plasma parameters measured between 0.3 and 1 AU. J. Geophys. Res. 87, 52–72. https://doi.org/10.1029/JA087iA01p00052.

Milillo, A., Fujimoto, M., Kallio, E., Kameda, S., Leblanc, F., Narita, Y., Cremonese, G., Laakso, H., Laurenza, M., Massetti, S., McKenna-Lawlor, S., Mura, A., Nakamura, R.,

Omura, Y., Rothery, D.A., Seki, K., Storini, M., Wurz, P., Baumjohann, W., Bunce, E.J., Kasaba, Y., Helbert, J., Sprague, A., 2010. Hermean Environment WG members, the BepiColombo mission: an outstanding tool for investigating the Hermean environment. Planet. Space Sci. 58, 40–60. https://doi.org/10.1016/j.pss.2008.06.005.

Milillo, A., Fujimoto, M., Murakami, G., Benkhoff, J., Zender, J., Aizawa, S., Dósa, M., Griton, L., Heyner, D., Ho, G., Imber, S.M., Jia, X., Karlsson, T., Killen, R.M., Laurenza, M., Lindsay, S.T., McKenna-Lawlor, S., Mura, A., Raines, J.M., Rothery, D.A., André, N., Baumjohann, W., Berezhnoy, A., Bourdin, P.A., Bunce, E.J., Califano, F., Deca, J., deÀ la Fuente, S., Dong, C., Grava, C., Fatemi, S., Henri, P., Ivanovski, S.L., Jackson, B.V., James, M., Kallio, E., Kasaba, Y., Kilpua, E., Kobayashi, M., Langlais, B., Leblanc, F., Lhotka, C., Mangano, V., Martindale, A., Massetti, S., Masters, A., Morooka, M., Narita, Y., Oliveira, J.S., Odstrcil, D., Orsini, S., Pelizzo, M.G., Plainaki, C., Plaschke, F., Sahraoui, F., Seki, K., Slavin, J.A., Vainio, R., Wurz, P., Barabash, S., Carr, C.M., Delcourt, D., Glassmeier, K.H., Grande, M., Hirahara, M., Huovelin, J., Korablev, O., Kojima, H., Lichtenegger, H., Livi, S., Matsuoka, A., Moissl, R., Moncuquet, M., Muinonen, K., Quèmerais, E., Saito, Y., Yagitani, S., Yoshikawa, I., Wahlund, J.E., 2020. Investigating mercury's environment with the two-spacecraft BepiColombo mission. Space Sci. Rev. 216, 93. https://doi.org/10.1007/s11214-020-00712-8.

Mukai, T., Yamakawa, H., Hayakawa, H., Kasaba, Y., Ogawa, H., 2006. Present status of the bepicolombo/Mercury magnetospheric orbiter. Adv. Space Res. 38, 578–582. https://doi.org/10.1016/j.asr. 2005.09.038 (Mercury, Mars and Saturn).

Müller, J., Simon, S., Motschmann, U., Schüle, J., Glaßmeier, K.-H., Pringle, G.J., 2011. A.i.k.e.f.: adaptive hybrid model for space plasma simulations. Comput. Phys. Commun. 182, 946–966. https://doi.org/10.1016/j.cpc.2010.12.033.

Müller, J., Simon, S., Wang, Y.-C., Motschmann, U., Heyner, D., Schüle, J., Ip, W.-H., Kleindienst, G., Pringle, G.J., 2012a. Origin of Mercury's double magnetopause: 3D hybrid simulation study with A.I.K.E.F. Icarus 218, 666–687. https://doi.org/10.1016/j.icarus.2011.12.028.

Müller, J., Simon, S., Wang, Y.-C., Motschmann, U., Heyner, D., Schüle, J., Ip, W.-H., Kleindienst, G., Pringle, G.J., 2012b. Origin of Mercury's double magnetopause: 3d hybrid simulation study with a.i.k.e.f. Icarus 218, 666–687. https://doi.org/10.1016/j.icarus.2011.12.028.

Ness, N.F., Behannon, K.W., Lepping, R.P., Whang, Y.C., 1975. The magnetic field of Mercury. J. Geophys. Res. 80, 2708–2716. https://doi.org/10.1029/JA080i019p02708, 1896-1977.

Orsini, S., Livi, S., Torkar, K., Barabash, S., Milillo, A., Wurz, P., di Lellis, A.M., Kallio, E., SERENA Team, 2010. SERENA: a suite of four instruments (ELENA, STROFIO, PICAM and MIPA) on board BepiColombo-MPO for particle detection in the Hermean environment. Planet. Space Sci. 58, 166–181. https://doi.org/10.1016/j.pss.2008.09.012.

Peng, I.B., Markidis, S., Laure, E., Johlander, A., Vaivads, A., Khotyaintsev, Y., Henri, P., Lapenta, G., 2015a. Kinetic structures of quasi-perpendicular shocks in global particle-in-cell simulations. Phys. Plasmas 22, 092109. https://doi.org/10.1063/1.4930212.

Peng, I.B., Markidis, S., Vaivads, A., Vencels, J., Amaya, J., Divin, A., Laure, E., Lapenta, G., 2015b. The formation of a magnetosphere with implicit particle-in-cell simulations. Procedia Comput. Sci. 51, 1178–1187. https://doi.org/10.1016/j.procs.2015.05.288 international Conference On Computational Science 2015: Computational Science at the Gates of Nature.

Powell, K.G., Roe, P.L., Linde, T.J., Gombosi, T.I., De Zeeuw, D.L., 1999. A solution-adaptive upwind scheme for ideal magnetohydrodynamics. J. Comput. Phys. 154, 284–309. https://doi.org/10.1006/jcph.1999.6299.

Raines, J.M., Gershman, D.J., Slavin, J.A., Zurbuchen, T.H., Korth, H., Anderson, B.J., Solomon, S.C., 2014. Structure and dynamics of Mercury's magnetospheric cusp: MESSENGER measurements of protons and planetary ions. J. Geophys. Res. (Space Phys.) 119, 6587–6602. https://doi.org/10.1002/2014JA020120.

Richer, E., Modolo, R., Chanteur, G.M., Hess, S., Leblanc, F., 2012. A global hybrid model for Mercury's interaction with the solar wind: case study of the dipole representation. J. Geophys. Res. (Space Phys.) 117, A10228. https://doi.org/10.1029/2012JA017898.

Roberts, D.A., Thieman, J., Génot, V., King, T., Gangloff, M., Perry, C., Wiegand, C., De Zeeuw, D., Fung, S.F., Cecconi, B., Hess, S., 2018. The SPASE data model: a metadata standard for registering, finding, accessing, and using heliophysics data obtained from observations and modeling. Space Weather 16, 1899–1911. https://doi.org/10.1029/2018SW002038.

Saito, Y., Sauvaud, J., Hirahara, M., Barabash, S., Delcourt, D., Takashima, T., Asamura, K., 2010. Scientific objectives and instrumentation of Mercury plasma particle experiment (mppe) onboard mmo. Planet. Space Sci. 58, 182–200. https://doi.org/10.1016/j.pss.2008. 06.003, comprehensive Science Investigations of Mercury: The scientific goals of the joint ESA/JAXA mission BepiColombo.

Sarantos, M., Slavin, J.A., 2009. On the possible formation of alfvén wings at mercury during encounters with coronal mass ejections. Geophys. Res. Lett. 36 https://doi.org/10.1029/2008GL036747. URL: https://agupubs.onlinelibrary.wiley.com/doi/abs/10.1029/2008GL036747.

Sarantos, M., Reiff, P.H., Hill, T.W., Killen, R.M., Urquhart, A.L., 2001. A Bx-interconnected magnetosphere model for Mercury. Planet. Space Sci. 49, 1629–1635. https://doi.org/10.1016/S0032-0633(01)00100-3.

Shue, J.H., Chao, J.K., Fu, H.C., Russell, C.T., Song, P., Khurana, K.K., Singer, H.J., 1997. A new functional form to study the solar wind control of the magnetopause size and shape. J. Geophys. Res. (Space Phys.) 102, 9497–9512. https://doi.org/10.1029/97JA00196.

Slavin, J.A., Acuña, M.H., Anderson, B.J., Baker, D.N., Benna, M., Gloeckler, G., Gold, R.E., Ho, G.C., Killen, R.M., Korth, H., Krimigis, S.M., McNutt, L.R., Nittler, L.R., Raines, J.M., Schriver, D., Solomon, S.C., Starr, R.D., Trávníček, P., Zurbuchen, T.H., 2008. Mercury's magnetosphere after MESSENGER's first flyby. Science 321, 85–89. https://doi.org/10.1126/science.1159040.

Slavin, J.A., Acuña, M.H., Anderson, B.J., Baker, D.N., Benna, M., Boardsen, S.A., Gloeckler, G., Gold, R.E., Ho, G.C., Korth, H., Krimigis, S.M., McNutt, R.L., Raines, J.M., Sarantos, M., Schriver, D., Solomon, S.C., Trávníček, P., Zurbuchen, T.H., 2009a. Messenger observations of magnetic reconnection in Mercury's magnetosphere. Science 324, 606–610. https://doi.org/10.1126/science.1172011.

Slavin, J.A., Anderson, B.J., Zurbuchen, T.H., Baker, D.N., Krimigis, S.M., Acuña, M.H., Benna, M., Boardsen, S.A., Gloeckler, G., Gold, R.E., Ho, G.C., Korth, H., McNutt Jr., R.L., Raines, J.M., Sarantos, M., Schriver, D., Solomon, S.C., Trávníček, P., 2009b. Messenger observations of mercury's magnetosphere during northward imf. Geophys. Res. Lett. 36 https://doi.org/10.1029/2008GL036158. URL: https://agupubs.onlinelibrary.wiley.com/doi/abs/10.1029/2008GL036158.

Slavin, J.A., Anderson, B.J., Baker, D.N., Benna, M., Boardsen, S.A., Gloeckler, G., Gold, R.E., Ho, G.C., Korth, H., Krimigis, S.M., McNutt, R.L., Nittler, L.R., Raines, J.M., Sarantos, M., Schriver, D., Solomon, S.C., Starr, R.D., Trávníček, P.M., Zurbuchen, T.H., 2010. Messenger observations of extreme loading and unloading of Mercury's magnetic tail. Science 329, 665–668. https://doi.org/10.1126/science.1188067.

Slavin, J.A., DiBraccio, G.A., Gershman, D.J., Imber, S.M., Poh, G.K., Raines, J.M., Zurbuchen, T.H., Jia, X., Baker, D.N., Glassmeier, K.-H., Livi, S.A., Boardsen, S.A., Cassidy, T.A., Sarantos, M., Sundberg, T., Masters, A., Johnson, C.L., Winslow, R.M., Anderson, B.J., Korth, H., McNutt Jr., R.L., Solomon, S.C., 2014. Messenger observations of Mercury's dayside magnetosphere under extreme solar wind conditions. J. Geophys. Res.: Space Phys. 119, 8087–8116. https://doi.org/10.1002/2014JA020319.

Slavin, J.A., Baker, D.N., Gershman, D.J., Ho, G.C., Imber, S.M., Krimigis, S.M., Sundberg, T., 2018. Mercury's dynamic magnetosphere. In: Solomon, S.C., Nittler, L.R., Anderson, B.J. (Eds.), Mercury: The View after MESSENGER. Cambridge University Press, pp. 461–496.

Slavin, J.A., Middleton, H.R., Raines, J.M., Jia, X., Zhong, J., Sun, W.-J., Livi, S., Imber, S.M., Poh, G.-K., Akhavan-Tafti, M., Jasinski, J.M., DiBraccio, G.A., Dong, C., Dewey, R.M., Mays, M.L., 2019. Messenger observations of disappearing dayside magnetosphere events at Mercury. J. Geophys. Res.: Space Phys. 124, 6613–6635. https://doi.org/10.1029/2019JA026892.

Trávníček, P., Hellinger, P., Schriver, D., 2007. Structure of Mercury's magnetosphere for different pressure of the solar wind: three dimensional hybrid simulations. Geophys. Res. Lett. 34, 5104. https://doi.org/10.1029/2006GL028518.

Trávníček, P.M., Schriver, D., Hellinger, P., Herčík, D., Anderson, B.J., Sarantos, M., Slavin, J.A., 2010. Mercury's magnetosphere: solar wind interaction for northward and southward interplanetary magnetic field: hybrid simulation results. Icarus 209, 11–22. https://doi.org/10.1016/j.icarus.2010.01.008.

Wang, Y.-C., Mueller, J., Motschmann, U., Ip, W.-H., 2010. A hybrid simulation of Mercury's magnetosphere for the MESSENGER encounters in year 2008. Icarus 209, 46–52. https://doi.org/10.1016/j.icarus.2010.05.020.

Whang, Y.C., 1977. Magnetospheric magnetic field of Mercury. J. Geophys. Res. 82, 1024–1030. https://doi.org/10.1029/JA082i007p01024, 1896-1977.

Wilson, I., Lynn, B., Stevens, M.L., Kasper, J.C., Klein, K.G., Maruca, B.A., Bale, S.D., Bowen, T.A., Pulupa, M.P., Salem, C.S., 2018. The Statistical Properties of Solar Wind Temperature Parameters Near 1 au. Astrophys. J. Suppl. 236, 41. https://doi.org/10.3847/1538-4365/aab71c arXiv:1802.08585.

Winslow, R.M., Anderson, B.J., Johnson, C.L., Slavin, J.A., Korth, H., Purucker, M.E., Baker, D.N., Solomon, S.C., 2013. Mercury's magnetopause and bow shock from MESSENGER Magnetometer observations. J. Geophys. Res. (Space Phys.) 118, 2213–2227. https://doi.org/10.1002/jgra.50237.

Winslow, R.M., Lugaz, N., Philpott, L., Farrugia, C.J., Johnson, C.L., Anderson, B.J., Paty, C.S., Schwadron, N.A., Asad, M.A., 2020. Observations of extreme ICME ram pressure compressing Mercury's dayside magnetosphere to the surface. Astrophys. J. 889, 184. https://doi.org/10.3847/1538-4357/ab6170 arXiv:1903.00577.

Xia, C., Teunissen, J., Mellah, I.E., Chané, E., Keppens, R., 2018. MPI-AMRVAC 2.0 for solar and astrophysical applications. Astrophys. J. Suppl. 234, 30. https://doi.org/10.3847/1538-4365/aaa6c8.

Yagi, M., Seki, K., Matsumoto, Y., 2009. Development of a magnetohydrodynamic simulation code satisfying the solenoidal magnetic field condition. Comput. Phys. Commun. 180, 1550–1557. https://doi.org/10.1016/j.cpc.2009.04.010.

Yagi, M., Seki, K., Matsumoto, Y., Delcourt, D.C., Leblanc, F., 2010. Formation of a sodium ring in Mercury's magnetosphere. J. Geophys. Res.: Space Phys. 115 https://doi.org/10.1029/2009JA015226.